Steam-created Grain Boundaries for Methane C-H Activation in Palladium Catalysts

Weixin Huang¹, Aaron C. Johnston-Peck², Trenton Wolter³, Wei-Chang D. Yang⁴, Lang Xu³, Jinwon Oh⁵, Benjamin A. Reeves¹, Chengshuang Zhou¹, Megan E. Holtz², Andrew A. Herzing², Aaron M. Lindenberg^{5,6}, Manos Mavrikakis³, Matteo Cargnello^{1,7*}

¹Department of Chemical Engineering, Stanford University, Stanford, CA 94305, USA

²Material Measurement Laboratory, National Institute of Standards and Technology, Gaithersburg, MD 20899, USA

³Department of Chemical and Biological Engineering, University of Wisconsin-Madison, Madison, WI 53706, USA

⁴Physical Measurement Laboratory, National Institute of Standards and Technology, Gaithersburg, MD 20899, USA

⁵Department of Materials Science and Engineering, Stanford University, Stanford, CA 94305, USA

⁶Stanford Institute for Materials and Energy Sciences, SLAC National Accelerator Laboratory, Menlo Park, CA 94025, USA

⁷SUNCAT Center for Interface Science and Catalysis, SLAC National Accelerator Laboratory, Menlo Park, CA 94025, USA

*Corresponding author: mcargnello@stanford.edu

Abstract

Defects may display high reactivity because the specific arrangement of atoms differs from crystalline surfaces. We demonstrate that high-temperature steam pretreatment of palladium catalysts provides a twelve-fold increase in the mass-specific reaction rate for C-H activation in methane oxidation compared to conventional pretreatments. Through a combination of experimental and theoretical methods, we demonstrate that an increase in the grain boundary density through crystal twinning is achieved during the steam pretreatment and oxidation and is responsible for the increased reactivity. The grain boundaries are highly stable during reaction and show specific rates at least two orders of magnitude higher than other sites on the Pd/Al₂O₃ catalysts. Theoretical calculations show that strain introduced by the defective structure can enhance C-H bond activation. Introduction of grain boundaries through laser ablation led to further rate increases.

One-Sentence Summary: Grain boundaries in palladium nanoparticles show two orders of magnitude increase in rates for methane combustion due to strain.

The catalytic activities of supported metal nanoparticles (NPs) can depend on their surface structure and the exposed surface sites (I-5). Specific types of surface sites, such as terrace sites, steps, grain boundaries (GBs), and metal-support interface sites, can be manipulated to improve catalytic activity (6, 7). For instance, tetrahexahedral platinum (Pt) NPs with high-index facets exhibit enhanced catalytic activity in electro-oxidation of formic acid and ethanol compared to Pt nanospheres (8). A silver catalyst with a high density of stacking faults showed superior activity and durability in the hydrogen evolution reaction (9).

Twin boundaries (TBs) and GBs are some of the most stable defects on metal surfaces and can be the active sites in certain electrocatalytic reactions (e.g. CO₂ electroreduction) (10–12). The improvement in performance resulted from the lattice strain induced by structural perturbations in the vicinity of the GBs at the catalyst surface (13), and this effect can lead to orders of magnitude higher catalytic rates (14). Although GBs have been recognized as promising defects for the activity of electrocatalysts, little is known about how they alter the catalytic properties in gas-phase heterogeneous reactions.

In this work, we show that steam pretreatment of a Pd/Al_2O_3 catalyst enhanced its methane combustion activity, with the mass-specific reaction rate increasing by ≈ 12 times compared to the same sample treated in O_2 . The extent of formation of TBs and GBs was correlated directly with the activity of these Pd catalysts. Density functional theory (DFT) calculations showed that changes in reactivity can be explained by surface strain present in the immediate vicinity of GBs. The specific active sites exhibited a two orders of magnitude higher intrinsic rate.

Uniform colloidal Pd NPs were deposited onto a commercial Al₂O₃ support (average diameter of 15 nm; see Fig. 1A for size distribution and images). The catalytic performance of the

Pd/Al₂O₃ catalyst was evaluated for methane combustion in the presence of steam (ramping the catalyst from 150 °C to determine the light-off temperature) for the pristine catalysts and after several gas pretreatments (O₂, H₂, Ar, and steam) at temperatures of 300 °C or higher (fig. S1A) (15). Negligible changes in light-off curves were observed relative to the pristine catalyst after conventional pretreatments (O₂, H₂, and Ar atmospheres) (fig. S1A) and had similar temperatures needed to achieve 50% conversion of CH₄ to CO₂ (T₅₀ values) of \approx 423 °C.

However, after a pretreatment in steam at 300 °C, the catalyst showed a noticeable improvement in catalytic activity that led to the lowest T_{50} value (fig. S1A). The Pd/Al₂O₃ catalyst was then pretreated in either steam or O₂ at increasing temperatures (300, 500, 600, and 700 °C). No catalytic enhancement was found for the catalyst pretreated in O₂ (fig. S1B), but after pretreatment in steam, catalytic activity improved with increasing pretreatment temperature up to 600 °C and showed no further change at 700 °C (Fig. 1B). For this catalyst, a T_{50} of \approx 373 °C was measured, which was 50 °C lower than the one treated in oxygen (Fig. 1D).

Co-feeding of steam in the reaction mixture usually has a detrimental effect on the methane combustion activity of Pd catalysts (16, 17), so it was surprising that the steam pretreatment could increase the activity of the catalyst. The higher performance after steam pretreatment was stable for at least five cycles (5 hours spent on stream, fig. S2). We also considered the variability in steam concentration and processing time during the pretreatment. The improved activity was achieved at a water concentration as low as 0.8 % (by volume) and did not change at increasing concentrations (fig. S3A). Changing the pretreatment duration from 0.5 h to 2 h did not change T₅₀ (fig. S3B). These experiments suggest that the pretreatment temperature was more important than its duration and steam concentration.

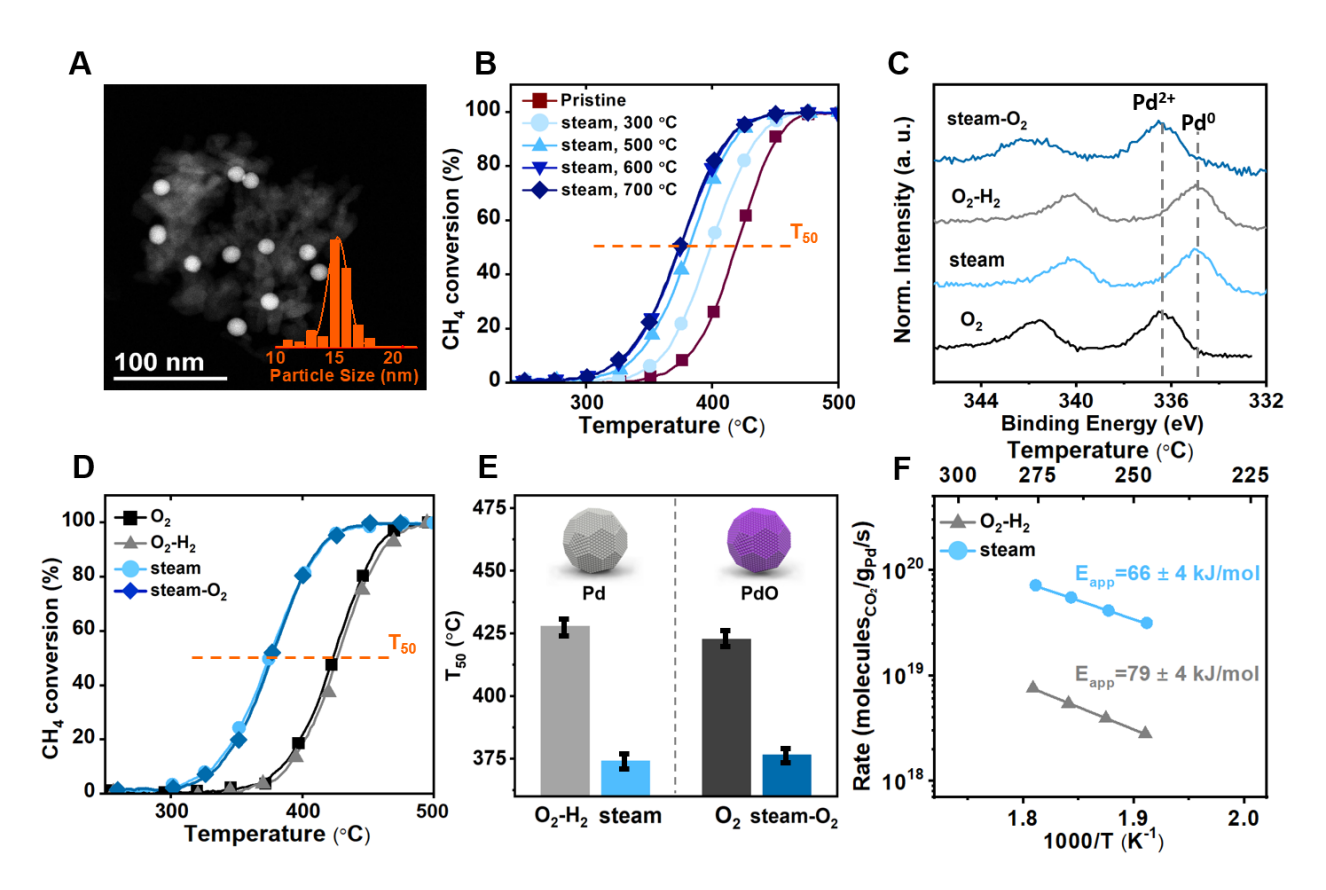


Fig. 1. Characterization and performance of Pd/Al₂O₃ catalysts upon different gas pretreatments. (A) Representative HAADF-STEM image of the pristine Pd/Al₂O₃ (inset: size distribution of Pd NPs). (B) Light-off curves for methane combustion (0.4% CH₄, 4.0% O₂, 4.2% H₂O, balance Ar) on pristine Pd/Al₂O₃ and after pretreatment in steam at increasing temperatures. (C) Pd 3d photoelectron spectra of Pd/Al₂O₃ after O₂ (600 °C), O₂-H₂, steam (600 °C), and steam-O₂ pretreatments. The spectral fittings are shown in fig. S5. (D) Light-off curves and (E) T₅₀ values of Pd/Al₂O₃ after O₂ (600 °C), O₂-H₂, steam (600 °C), and steam-O₂ pretreatments. Error bars represent the minimum and maximum measured values of at least three repeated experiments. (F) Arrhenius plots of methane combustion on Pd/Al₂O₃ after O₂-H₂ pretreatment and steam pretreatment (600 °C).

Using high-angle annular dark-field scanning transmission electron microscopy (HAADF-STEM) analysis, we confirmed that there was no appreciable change in NP size distributions after any of the treatments (fig. S4), so the improved catalytic activity was not the result of particle sintering or redispersion. X-ray photoelectron spectroscopy (XPS) measurements demonstrated that in the O₂-pretreated catalyst, Pd 3d_{5/2} peak was located at 336.6 eV (Fig. 1C and fig. S5), consistent with PdO phase. The steam-pretreated catalyst showed the peak at 335.0 eV attributable to metallic Pd(0), which was consistent with x-ray diffraction (XRD) data (fig. S6). In any case, the catalysts were oxidized under reaction conditions (see below).

There is still a debate as to whether Pd, PdO, or a Pd/PdO mixed phase is the active phase for methane combustion (18). To fairly compare catalysts with the same oxidation state, a Pd/Al₂O₃ sample was prepared through sequential oxygen and hydrogen treatments [labeled as O₂-H₂-pretreated Pd/Al₂O₃, (15)] to convert the Pd oxide phase into metallic Pd, as confirmed by XPS (Fig. 1C). However, the activity for this sample was similar to the one pretreated exclusively in O₂ and much lower than the steam-pretreated catalyst (Fig. 1, D and E). We subjected the steam-pretreated sample to an oxygen treatment [labeled as steam-O₂-pretreated Pd/Al₂O₃, (15)] to convert the metallic Pd phase into PdO (as confirmed by XPS, Fig. 1C) and test whether the oxidation would reduce its activity to that of the oxidized sample. No evident activation/deactivation in light-off performance was found as compared to the steam-pretreated sample (Fig. 1D). This demonstrated that the initial Pd oxidation state before catalysis did not correlate with the methane oxidation activity of the samples, and steam pretreatment improved the Pd activity regardless of its initial oxidation state.

Reaction rates were measured for these various Pd/Al_2O_3 catalysts. Steam was not added to the reaction mixture to avoid catalyst changes during kinetic experiments (fig. S7). The 600 °C steam-pretreated catalyst had a \approx 12 times higher mass-specific rate than the O_2 -H₂-pretreated catalyst (Fig. 1F). Activating the first C-H bond is recognized as the rate-limiting step in methane

oxidation, and Arrhenius plots showed an apparent activation energy for the O_2 - H_2 -pretreated catalyst of 79 ± 4 kJ·mol⁻¹, in agreement with previous studies (19). The steam-pretreated catalyst had lower activation energy (66 ±4 kJ·mol⁻¹). The two samples showed similar values of the prefactor ($\approx 3 \times 10^{26}$ molecules_{CO2}/g_{Pd}/s).

The effect of PdO reducibility state was explored with methane temperature-programmed reduction (CH₄-TPR, fig. S8A). Whereas methane oxidation was observed at \approx 190 °C for the steam-pretreated catalyst, the temperature shifted up to \approx 215 °C for the O₂-pretreated catalyst, consistent with the light-off curves (Fig. 1D). In temperature-programmed Pd oxidation (O₂-TPO) experiments, O₂ uptake was observed at \approx 295 °C for the steam-pretreated catalyst versus \approx 330 °C for the O₂-pretreated one (fig. S8B), in line with DFT calculations (see below). Thus, the Pd phase in the steam-pretreated catalyst was more easily oxidized and reduced by O₂ and CH₄, respectively, and could be more active in methane oxidation.

Changes in the support after steam treatment, including support hydroxylation, can promote reactivity of supported metal phases (20). We treated the alumina support in steam before depositing Pd NPs (15), but this sample showed an even higher T₅₀ than that of conventional Pd/Al₂O₃ with the same NP size (fig. S9). The decreased activity could have been caused by different metal-support interactions with hydroxylated alumina. Also, Pd/SiO₂ catalysts showed the same improvement in activity when treated in steam versus oxygen or oxygen-hydrogen atmospheres (fig. S10). Activity improvement could result from catalyst synthesis by-products being removed from the surface by the steam treatment. Phosphorus is an impurity in the initial Pd NPs. However, it was mostly removed after steam or O₂-H₂ treatments, and there was no difference in its concentration between the samples (fig. S11 and table S2). These results suggest that the observed activity enhancement is related to structural changes in the Pd NPs.

We used HAADF-STEM to characterize the structure of the supported metallic Pd NPs (Fig. 2 and figs. S12 to S17). Oxidized Pd NPs underwent drastic electron-beam induced changes and could not be investigated in detail. The pristine Pd NPs on alumina mostly had an amorphous structure (fig. S12). However, after being treated in steam or O₂-H₂, the NPs crystallized and became highly faceted.

Different Pd exposed facets upon different gas pretreatments could account for the changes in reactivity (fig. S17). The distances from the particle center to the outermost surface planes were measured (table S3), and the corresponding three-dimensional crystal shape was derived by using the Wulff construction. From the Wulff shape, the occurrence of different types of surface facets was extracted (fig. S18). Although samples showed different fractions of exposed facets, no trend correlated with the difference in catalyst activity (figs. S18 and S19), nor did the presence of voids in the NPs created by Kirkendall effects (figs. S12 to S15 and table S4). A similar procedure was used to analyze oxidized NPs, and although the beam sensitivity allowed measurements of only few of them, comparable ratios of PdO {110} and {101} facets were observed (fig. S20 and table S5).

Both the steam- and O_2 -H₂-pretreated samples presented TBs that lay parallel to {111} planes (also referred to as $\Sigma 3$ {111} TBs, arrows in Fig. 2, A, B, and E). Separated by a coherent TB, the surface structure shows a symmetrical lattice arrangement with an ABC|CBA stacking sequence. The fast Fourier-Transform (FFT) diffractograms in Fig. 2J showed two sets of patterns, in which the (1 $\overline{1}1$), (200) spots in grain G2 are mirrored, across the plane parallel to ($\overline{1}1$), by ($\overline{1}11$), (00 $\overline{2}$) in grains G1 and G3, forming a typical coherent TB pattern.

To assess the relation between the presence of TBs and catalytic activity, we measured the TB surface density, which was taken to be the sum of the TB surface length over all measured NPs divided by the sum of the NP surface areas (15). We used experimental data on samples after different treatments to estimate the TB density to be \approx 58 μ m⁻¹ for the steam-treated sample and \approx 15 μ m⁻¹ for the O₂-H₂-pretreated sample (Fig. 2K and table S6). This result correlated well with the observed catalytic activity trend.

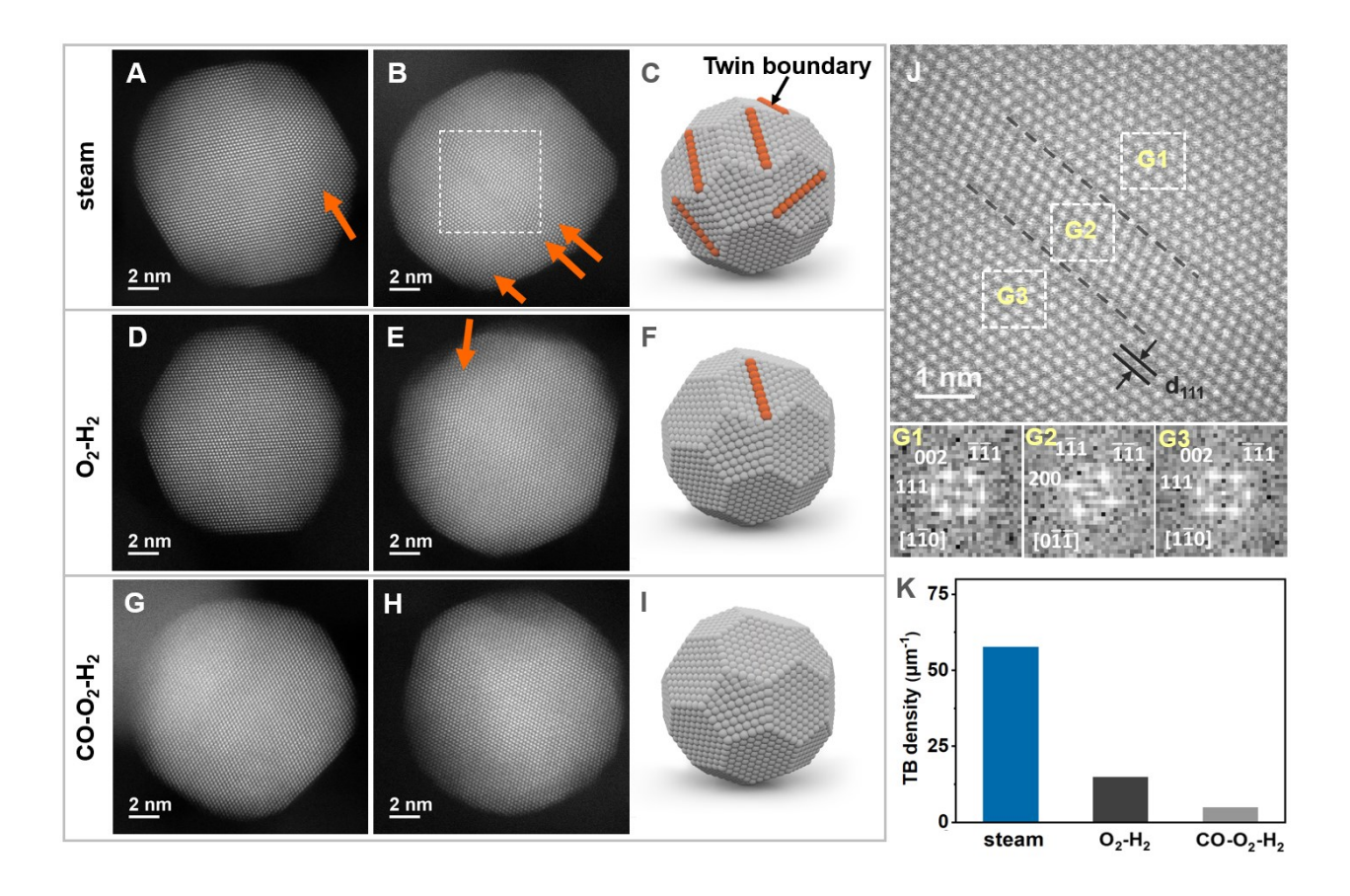


Fig. 2. Microstructure investigation. Atomic-resolution HAADF-STEM images of (A and B) steam-pretreated (600 °C) Pd/Al₂O₃, (D and E) O₂-H₂-pretreated Pd/Al₂O₃, (G and H) CO-O₂-H₂-pretreated Pd/Al₂O₃. (C, F and I) Schematic of the TB density change in Pd NPs after different gas pretreatments. (J) The area marked by the boxes in (B), revealing the detailed arrangements of Pd atoms. The dash lines

highlight Σ3 {111} TBs. Corresponding FFT images of grains (G1, G2, and G3) labeled in the top panel. (K) TB density statistical histogram of Pd/Al₂O₃ after steam (600 °C), O₂-H₂, and CO-O₂-H₂ treatment.

To confirm the role of TB density, a pristine Pd/Al₂O₃ sample was subjected to dilute CO treatment to cause Pd NPs to restructure into vicinal stepped surfaces (4) and decrease TB formation. The sample was further subjected to O₂ and H₂ treatments to remove the carbon coating induced by the CO treatment (fig. S21), reduce the Pd to metallic state, and create a fully accessible and active Pd surface [labeled as CO-O₂-H₂-pretreated Pd/Al₂O₃, (15)]. No appreciable change in NP size was seen in TEM images, and XPS confirmed the metallic state of Pd (fig. S22). The CO-O₂-H₂-pretreated sample indeed had low TB density of \approx 4.9 μ m⁻¹, as revealed by high-resolution HAADF-STEM images (Fig. 2, G to I and fig. S15), was also less active than both the steam-pretreated catalyst and the O₂-H₂ catalyst, with higher T₅₀ of \approx 446 °C (Fig. 3A and fig. S23).

These results were consistent with the observed correlation of the increased activity of the Pd/Al_2O_3 catalysts with TBs, and the lack of TB formation under O_2 , H_2 , or CO atmospheres (Fig. 3B). We calculated an intrinsic reaction rate if the atoms at the TB for the measured TB density in the steam-pretreated sample accounted for the increase in rate (15). This rate was ≈ 785 times greater than that on the in-plane Pd atoms.

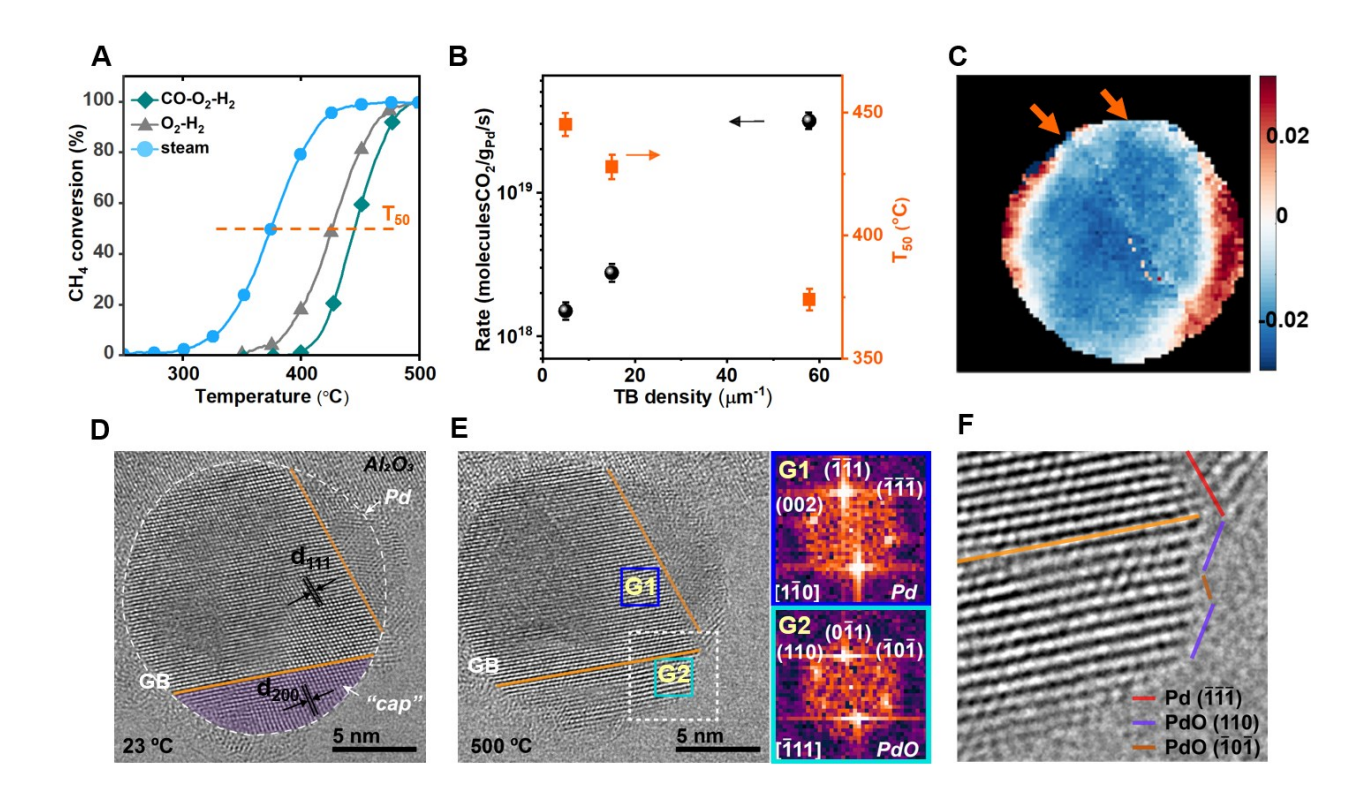


Fig. 3. Identifying TBs as the origin of increased catalytic activity and exploring their thermal stability. (A) Light-off curves of Pd/Al₂O₃ after steam (600 °C), O₂-H₂ and CO-O₂-H₂ pretreatments. (B) Relationship between reaction rate/T₅₀ and TB density. (C) Representative strain mapping for an individual Pd NP in the stream-pretreated catalyst relative to the reference values in the horizontal direction. The arrows denote the TBs. (D) and (E) Representative environmental TEM (E-TEM) images of the same Pd nanoparticle in the steam-pretreated Pd/Al₂O₃ sample that was exposed to O₂ at 23 °C and 500 °C, respectively, with the twin/grain boundaries highlighted by orange lines. FFT diffractograms (insets in (E)) indicating that the "cap" region separated by GB is preferentially oxidized at 500 °C. (F) Zoom-in of the area marked by the white dashed box in (E) showing the exposed Pd and PdO facets in the vicinity of the GB (orange line).

Enhanced catalytic activity associated with TBs could be related to strain effects given the presence of the GB. The exit-wave power-cepstrum (EWPC) transform was applied to scanning nanobeam electron diffraction data to explore the distribution of lattice strain in the steam- and CO-O₂-H₂-pretreated Pd/Al₂O₃ catalyst (21). The strain values are relative to a reference value (Lagrange strain), which was measured from the sum of all the diffraction patterns for individual NPs (Fig. 3C). Analysis revealed a radial lattice expansion near surfaces in both stream- and CO-O₂-H₂-pretreated samples regardless of the presence of a TB, and no correlation between the presence of a TB and a change in strain was identified in the Pd samples (figs. S24 and S25). A previous report analyzing atomic resolution images of supported Pt NPs reported a 1% to 2% expansion in the lattice planes immediately adjacent to the TB (22). The difference in results reported here could originate from the material system and synthesis, or from the lower spatial resolution of the strain routine implemented here lacking sensitivity. However, analysis of the prereaction NPs may not be sufficient given restructuring under reaction conditions and oxidation of the metallic surface.

Thus, we determined the thermal stability of the TBs under oxidizing conditions using environmental transmission electron microscopy (E-TEM). Initially, the Pd/Al₂O₃ was exposed to an O₂ environment at a pressure of \approx 0.87 Pa at room temperature (Supplementary Video 1). The catalyst was heated at a rate of 100 °C·s⁻¹ and stabilized at \approx 500 °C (Supplementary Video 2). We detected no apparent boundary segregation or disappearance as annealing temperature increased (from Fig. 3D to E). Instead, surface oxidation on the NP was observed during this process: the "cap" separated by the {111} TB was preferentially oxidized (Fig. 3, E and F), suggesting that the TB may promote oxygen dissociation and serve as the precursor structure to the formation of a GB between the Pd core and the surface PdO region. A slower heating rate experiment (200 °C·min⁻¹)

showed that the "cap" region was preferentially oxidized at \approx 391 °C in the same O_2 environment (fig. S26). We confirm the PdO phase formation based on the FFT diffractogram (bottom inset of Fig. 3E) that matches well with tetragonal PdO and suggests the oxidized "cap" region is oriented close to the $[\bar{1}11]$ zone axis. The PdO surface is bounded by the (110) and ($\bar{1}0\bar{1}$) facets (Fig. 3F). A time series of consecutive frames (each 2.5 sec apart) selected from Supplementary Video 2 shows the dynamic nature of the PdO facets in the oxidizing environment, with the PdO (110) surface replaced by the ($\bar{1}0\bar{1}$) surface (second frame) before reappearing (third frame) (as shown in fig. S27).

The E-TEM identification explained the O₂-TPO data, in which the steam-pretreated catalyst oxidized at a lower temperature compared to the O₂-pretreated catalyst. We conclude that the original TB transformed into a general GB, indicating that these planar defects were maintained in an oxidizing condition at a high temperature of at least 500 °C. The conversion of Pd to PdO transformed the crystalline lattice from cubic to tetragonal.

There can be multiple reasons as to why the TBs might lead to an increased reaction rate. TBs may impart structural irregularities that induce reconstruction of the PdO surface (23). Further, linear and/or point defects at the vicinity of the TB can lead to improved C-H bond activation(24). Alternatively, the oxidation of the metal surface may generate strain in the Pd/PdO heterostructure and in the fully oxidized PdO NP containing the GB. We explored this latter possibility in detail using DFT.

We performed planewave DFT calculations for the dissociation of O₂ on Pd(111) and a TB model between two Pd(111) terraces (fig. S28). The binding energy of O₂ was calculated to be - 1.07 eV and -1.19 eV on Pd(111) and the TB model, respectively. The O₂ dissociation barriers

were calculated to be 0.66 eV and 0.49 eV on Pd(111) and the TB model, respectively. Overall, when referenced to gas-phase O₂, the O₂ dissociation transition state is 0.29 eV more stable on the TB model than on Pd(111) (which corresponds to ~150-fold difference in rate at 400 °C). These results indicate that the presence of twin boundaries will increase the O₂ population on the surface and facilitate O₂ dissociation relative to the Pd(111) facet, both suggesting that PdO formation is accelerated in the vicinity of twin boundaries. These results are in line with the CH₄-TPR analysis reported above.

Planewave DFT calculations were also performed to assess the effect of strain generated by the GBs on the activity of the catalyst for the first C-H bond-breaking step in methane combustion, known to be rate-determining given the rate orders for methane and oxygen of \approx +1 and 0, respectively (fig. S29). PdO(110) and PdO(101) were chosen because the oxidized phase formed under reaction conditions (Fig. 3E) and pre-oxidation of the NPs did not hinder catalytic activity (Fig. 1D). These facets were specifically chosen because they were observed with E-TEM (Fig. 3F). The catalyst surfaces were modeled as bulk PdO surfaces because the NPs that were placed under reaction conditions were measured to have PdO phases that were at least 4 nm thick, which corresponds to approximately 13 atomic layers. At this PdO thickness, there should be a sufficient number of PdO layers so that they would resemble the properties of a bulk PdO surface, whereas the contribution from the supporting metallic Pd substrate is effectively screened.

Gibbs free energy (Δ G) diagrams and energy-optimized structures for adsorbed CH₄*, the transition states (TS), and the final states (CH₃* + H*) were computed (Fig. 4, A to D). The calculation of the Δ G assumed a temperature of 400 °C, at which the largest difference in methane conversion between steam-pretreated and O₂-pretreated catalysts was observed (Fig. 1D). Calculations were performed for each surface at -5% (i.e., 5% compressive), 0%, and +5% (i.e.,

5% expansive) strain, so that the effects of both types of strain were explored and a trend could be established between the reactivity and the applied strain level.

The ΔG of adsorbed methane on PdO(101) with -5, 0, and 5% applied strain were -0.03, -0.07, and -0.25 eV, respectively (Fig. 4A). These values indicate that CH₄ binds stronger to the surface with expansive strain, which is consistent with previous observed strain effects on metallic surfaces(25). The TS ΔG relative to gas-phase CH₄ were 0.89, 0.85, and 0.63 eV for -5, 0, and 5% applied strain, respectively. These energy values are effectively the ΔG differences between the C-H activation barrier and the desorption barrier of adsorbed CH₄. Expansive strain could increase the activity for C-H activation (as opposed to CH₄ desorption) on the PdO(101) surface.

To give a sense for the magnitude of this effect, a difference of ca. 0.13 eV in activation energy corresponds to one order of magnitude change in reaction rate constant at 400 °C. Thus, imposing a 5% expansive strain on PdO(101) would yield an intrinsic reactivity enhancement corresponding to a 0.22 eV TS energy difference, and a coverage term enhancement due to stronger CH₄ binding by 0.18 eV. Combined, this leads to \approx 3 orders of magnitude in intrinsic rate enhancement for the expansively strained PdO(101) surface, an estimate that is near the factor of 785 estimated from our experiments.

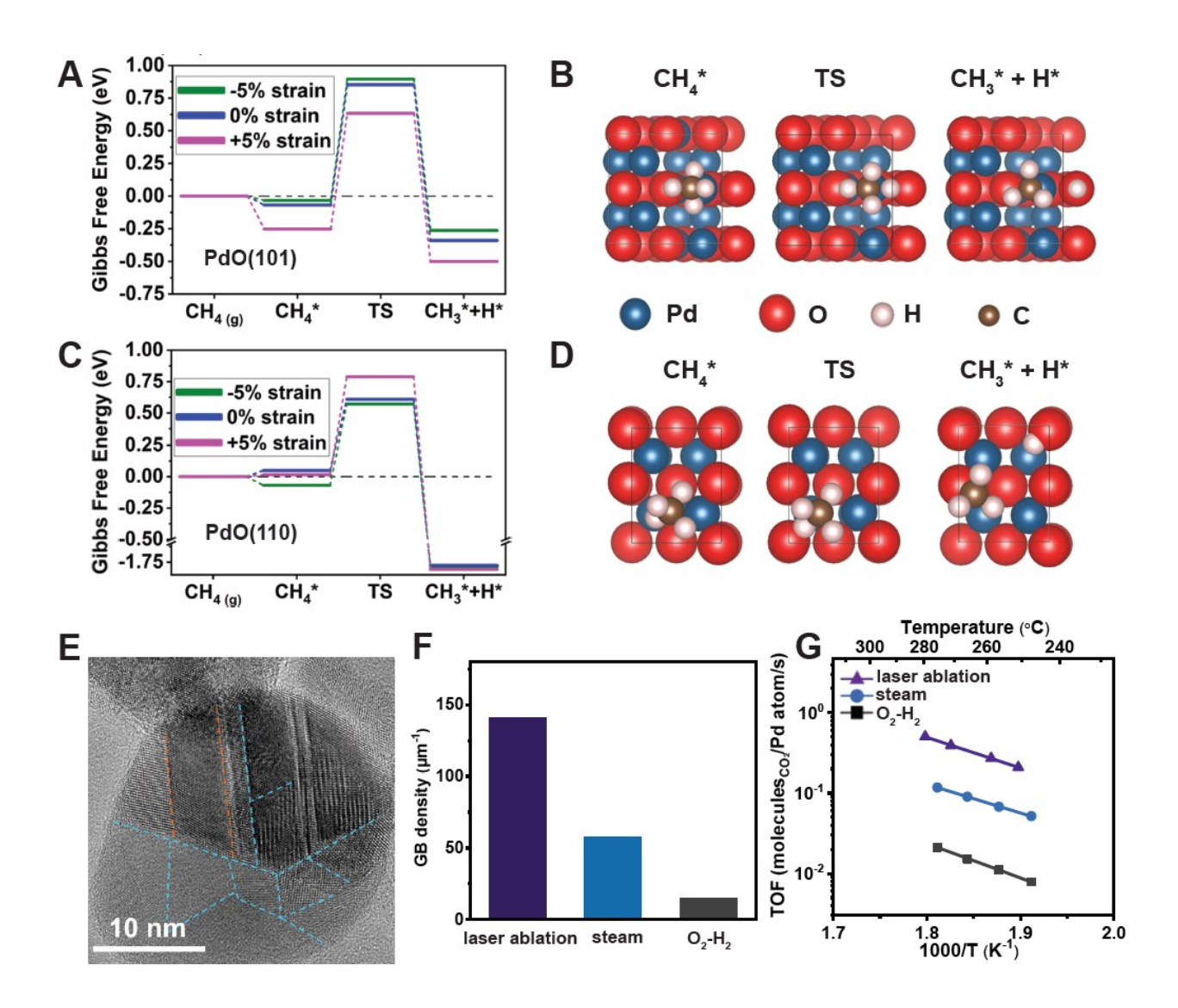


Fig. 4. Theoretical calculations for the effect of surface strain on the C-H breaking ΔG and GB density effect investigation. (A) and (C) Calculated free energy diagrams for breaking the first C-H bond in CH₄ on PdO(101) and PdO(110), respectively. The ΔG were calculated using a temperature of 400 °C and referenced a clean surface and gas-phase CH₄ at infinite separation. (B) and (D) Top view of structures for adsorbed CH₄ (CH₄*), TS, and co-adsorbed CH₃ and H (CH₃* + H*) on PdO(101) and PdO(110), respectively (side views are shown in fig. S32). Light black rectangle denotes the unit cell. (E) High-resolution TEM image of laser ablation-generated Pd NPs. The orange dash lines highlight Σ3{111} TBs and the blue dash lines highlight GBs. (F) GB density statistical histogram of laser-generated Pd/Al₂O₃ and

Pd/Al₂O₃ after steam (600 °C) and O₂-H₂ pretreatments. (G) Arrhenius plots of methane combustion of laser-generated Pd/Al₂O₃ and Pd/Al₂O₃ after steam (600 °C) and O₂-H₂ pretreatments.

For comparison, the ΔG diagram for methane activation on the PdO(110) facet was also calculated (Fig. 4C). The reactivity of this surface was probed at its oxygen-termination that corresponds to a lower surface energy compared to its Pd-termination under the experimental conditions used in this study (26). The application of expansive or compressive strain did not show a large effect on the binding energy of CH₄* or CH₃* + H* on this surface, where only narrow ranges of variances in the energies of CH₄* (0.05 eV) and CH₃* + H* (0.03 eV) were observed (Fig. 4C).

The TS energies on the PdO(110) surface showed a different trend than that observed on the PdO(101) surface as expansive or compressive strain was applied. The TS energies are 0.57, 0.61, 0.79 eV for -5, 0, and 5% applied strain, respectively (Fig. 4C). These results suggest that a 5%-compressed PdO(110) could increase intrinsic reactivity corresponding to a total of \approx 0.09 eV lower Δ G, which is less than an order or magnitude at 400 °C, compared to 0% strain on that facet. Expansive strain would decrease reactivity on that facet.

The DFT results for PdO(101) and PdO(110) together demonstrate that a strained surface causes higher C-H activation rate. As mentioned previously in the E-TEM experiment, the PdO phase tended to form a "cap" region on one side of the GB, so the PdO phase could undergo compressive or expansive strain created by GBs, which, in turn, could increase reactivity. This idea is consistent with the experimental results showing higher activity for NPs that have a higher number of TBs.

Our DFT results suggest that the enhanced activity for the steam-pretreated Pd catalyst stems from a concerted effect of PdO formation and local strain caused by the presence of GBs. Based on the reactivity enhancement estimates calculated on the stretched Pd(101) and on the compressed PdO(110), and the respective comparisons with experimental rate measurements, we conclude that stretched Pd(101) is likely the dominant active site on the steam-pretreated catalysts. This assertion offers a potential avenue for improving Pd methane oxidation catalysts through better control of the facets and strain during PdO growth.

Activity enhancement by steam pretreatment was not exclusive of the Pd(15 nm)/Al₂O₃ catalyst. The same pretreatment-dependent activity profiles were observed in a Pd/Al₂O₃ catalyst prepared by conventional wet impregnation, and Pd/Al₂O₃ catalysts prepared from 8 and 12 nm colloidal Pd NPs (figs. S33 to S35). In all these cases, the steam-pretreated catalysts exhibited higher activity than the O₂-pretreated catalysts. The NPs with a larger size showed greater improvement in rates upon the steam treatment (fig. S36). This observation may be explained by the more energetically favorable formation of TBs in larger NPs that can more easily accommodate defects. Despite a lower magnitude in rate increase likely caused by the smaller NP sizes and a less uniform surface structure in the wet-impregnated catalyst, these experiments confirm the generality of the effect of steam pretreatment on Pd catalysts.

Finally, the identification of GBs as highly active sites for methane combustion provides the opportunity to engineer Pd/Al₂O₃ catalysts for even improved reactivity if the density of such defects can be increased. With this goal in mind, a laser ablation process was used to fabricate NPs rich in GBs (Fig. 4, E and F, and figs. S37 and S38) following previous reports (9) that were deposited on the same alumina used for the colloidal NPs. As predicted by our observations, the turnover frequency (TOF) of the laser ablation-generated Pd/Al₂O₃ catalyst was four times higher

than that of the steam-pretreated Pd(15 nm)/Al₂O₃ catalyst, and hence nearly twenty-five times higher than a conventional catalyst pretreated in just oxygen and hydrogen (Fig. 4G and table S7). These results may provide not only a general strategy for the rational design of the surface structure in heterogeneous nanocatalysts, but also can help explain previous work on Pd-based catalysts for methane combustion that demonstrated improved reactivity upon aging or disparate thermal treatments (27).

REFERENCES AND NOTES

- 1. P. Nolte, A. Stierle, N. Y. Jin-Phillipp, N. Kasper, T. U. Schulli, H. Dosch, Shape changes of supported Rh nanoparticles during oxidation and reduction cycles. *Science* **321**, 1654–1658 (2008). doi:10.1126/science.1160845
- 2. B. Hammer, Special sites at noble and late transition metal catalysts. *Top. Catal.* **37**, 3–16 (2006). doi:10.1007/s11244-006-0004-y
- 3. F. F. Tao, L. Nguyen, S. Zhang, Y. Li, Y. Tang, L. Zhang, A. I. Frenkel, Y. Xia, M. Salmeron, Formation of second-generation nanoclusters on metal nanoparticles driven by reactant gases. *Nano Lett.* **16**, 5001–5009 (2016). doi:10.1021/acs.nanolett.6b01718
- 4. T. Avanesian, S. Dai, M. J. Kale, G. W. Graham, X. Pan, P. Christopher, Quantitative and atomic-scale view of CO-induced Pt nanoparticle surface reconstruction at saturation coverage via DFT calculations coupled with in Situ TEM and IR. *J. Am. Chem. Soc.* **139**, 4551–4558 (2017). doi:10.1021/jacs.7b01081

- L. Wang, Z. Zeng, W. Gao, T. Maxson, D. Raciti, M. Giroux, X. Pan, C. Wang, J. Greeley,
 Tunable intrinsic strain in two-dimensional transition metal electrocatalysts. *Science* 363, 870–874 (2019). doi: 10.1126/science.aat8051
- 6. P. P. Sharma, J. Wu, R. M. Yadav, M. Liu, C. J. Wright, C. S. Tiwary, B. I. Yakobson, J. Lou, P. M. Ajayan, X. D. Zhou, Nitrogen-doped carbon nanotube arrays for high-efficiency electrochemical reduction of CO₂: on the understanding of defects, defect density, and selectivity. *Angew. Chem. Int. Ed.* **54**, 13701–13705 (2015). doi:10.1002/anie.201506062
- 7. Y. Li, F. Cui, M. B. Ross, D. Kim, Y. Sun, P. Yang, Structure-Sensitive CO₂ electroreduction to hydrocarbons on ultrathin 5-fold twinned copper nanowires. *Nano Lett.* 17, 1312–1317 (2017). doi:10.1021/acs.nanolett.6b05287
- 8. N. Tian, Z. Y. Zhou, S. G. Sun, Y. Ding, L. W. Zhong, Synthesis of tetrahexahedral platinum nanocrystals with high-index facets and high electro-oxidation activity. *Science* **316**, 732–735 (2007). doi:10.1126/science.1140484
- 9. Z. Li, J. Y. Fu, Y. Feng, C. K. Dong, H. Liu, X. W. Du, A silver catalyst activated by stacking faults for the hydrogen evolution reaction. *Nat. Catal.* **2**, 1107–1114 (2019). doi:10.1038/s41929-019-0365-9
- M. Zhao, L. Xu, M. Vara, A. O. Elnabawy, K. D. Gilroy, Z. D. Hood, S. Zhou, L. Figueroa-Cosme, M. Chi, M. Mavrikakis, Y. Xia, Synthesis of Ru icosahedral nanocages with a face-centered-cubic structure and evaluation of their catalytic properties. *ACS Catal.* 8, 6948–6960 (2018). doi:10.1021/acscatal.8b00910
- 11. X. Feng, K. Jiang, S. Fan, M. W. Kanan, Grain-boundary-dependent CO₂ electroreduction

- activity. J. Am. Chem. Soc. 137, 4606–4609 (2015). doi:10.1021/ja5130513
- 12. C. W. Li, J. Ciston, M. W. Kanan, Electroreduction of carbon monoxide to liquid fuel on oxide-derived nanocrystalline copper. *Nature* **508**, 504–507 (2014). doi:10.1038/nature13249
- 13. R. G. Mariano, K. McKelvey, H. S. White, M. W. Kanan, Selective increase in CO₂ electroreduction activity at grain-boundary surface terminations. *Science* **358**, 1187–1192 (2017). doi:10.1126/science.aao3691
- C. Tang, J. Shi, X. Bai, A. Hu, N. Xuan, Y. Yue, T. Ye, B. Liu, P. Li, P. Zhuang, J. Shen,
 Y. Liu, Z. Sun, CO₂ reduction on copper's twin boundary. *ACS Catal.* 10, 2026–2032 (2020). doi:10.1021/acscatal.9b03814
- 15. See the supplementary materials.
- D. Ciuparu, M. R. Lyubovsky, E. Altman, L. D. Pfefferle, A. Datye, Catalytic combustion of methane over palladium-based catalysts. *Catal. Rev.: Sci. Eng.* 44, 593–649 (2002). doi:10.1081/CR-120015482
- 17. R. Gholami, M. Alyani, K. J. Smith, Deactivation of Pd catalysts by water during low temperature methane oxidation relevant to natural gas vehicle converters. *Catalysts* **5**, 561–594 (2015). doi:10.3390/catal5020561
- 18. Y. H. Chin, C. Buda, M. Neurock, E. Iglesia, Consequences of metal-oxide interconversion for C-H bond activation during CH₄ reactions on Pd catalysts. *J. Am. Chem. Soc.* **135**, 15425–15442 (2013). doi:10.1021/ja405004m

- J. J. Willis, E. D. Goodman, L. Wu, A. R. Riscoe, P. Martins, C. J. Tassone, M. Cargnello, Systematic identification of promoters for methane oxidation catalysts using size- and composition-controlled Pd-based bimetallic nanocrystals. *J. Am. Chem. Soc.* 139, 11989– 11997 (2017). doi:10.1021/jacs.7b06260
- L. Nie, D. Mei, H. Xiong, B. Peng, Z. Ren, X. I. P. Hernandez, A. DeLaRiva, M. Wang, M. H. Engelhard, L. Kovarik, A. K. Datye, Y. Wang, Activation of surface lattice oxygen in single-atom Pt/CeO₂ for low-temperature CO oxidation. *Science* 358, 1419–1423 (2017). doi:10.1126/science.aao2109
- 21. E. Padgett, M. E. Holtz, P. Cueva, Y. T. Shao, E. Langenberg, D. G. Schlom, D. A. Muller, The exit-wave power-cepstrum transform for scanning nanobeam electron diffraction: robust strain mapping at subnanometer resolution and subpicometer precision. *Ultramicroscopy* **214**, 112994 (2020). doi:10.1016/j.ultramic.2020.112994
- 22. T. Nilsson Pingel, M. Jørgensen, A. B. Yankovich, H. Grönbeck, E. Olsson, Influence of atomic site-specific strain on catalytic activity of supported nanoparticles. *Nat. Commun.* **9**, 1–9 (2018). doi:10.1038/s41467-018-05055-1
- N. M. Martin, M. Van den Bossche, A. Hellman, H. Grönbeck, C. Hakanoglu, J. Gustafson,
 S. Blomberg, N. Johansson, Z. Liu, S. Axnanda, J. F. Weaver, E. Lundgren, Intrinsic Ligand
 Effect Governing the Catalytic Activity of Pd Oxide Thin Films. ACS Catal. 4, 3330–3334
 (2014). doi:10.1021/cs5010163
- 24. H. H. Kan, J. F. Weaver, Mechanism of PdO thin film formation during the oxidation of Pd(1 1 1). *Surf. Sci.* 603, 2671–2682 (2009). doi:10.1016/j.susc.2009.06.023

- 25. M. Mavrikakis, B. Hammer, J. K. Nørskov, Effect of Strain on the Reactivity of Metal Surfaces. *Phys. Rev. Lett.* **81**, 2819–2822 (1998). doi:10.1103/PhysRevLett.81.2819
- J. Rogal, K. Reuter, M. Scheffler, Thermodynamic stability of PdO surfaces. *Phys. Rev. B* Condens. Matter Mater. Phys. 69, 075421 (2004). doi:10.1103/PhysRevB.69.075421
- 27. O. Demoulin, G. Rupprechter, I. Seunier, B. Le Clef, M. Navez, P. Ruiz, Investigation of parameters influencing the activation of a Pd/γ-alumina catalyst during methane combustion. *J. Phys. Chem. B* **109**, 20454–20462 (2005). doi:10.1021/jp051874g
- 28. M. Cargnello, C. Chen, B. T. Diroll, V. V. T. Doan-Nguyen, R. J. Gorte, C. B. Murray, Efficient removal of organic ligands from supported nanocrystals by fast thermal annealing enables catalytic studies on well-defined active phases. *J. Am. Chem. Soc.* **137**, 6906–6911 (2015). doi: 10.1021/jacs.5b03333
- 29. B. Schaffer, How To Script Digital micrograph scripting handbook by bernhard schaffer, (available at http://digitalmicrograph-scripting.tavernmaker.de/HowToScript_index.htm).
- 30. J. Schindelin, I. Arganda-Carreras, E. Frise, V. Kaynig, M. Longair, T. Pietzsch, S. Preibisch, C. Rueden, S. Saalfeld, B. Schmid, J. Y. Tinevez, D. J. White, V. Hartenstein, K. Eliceiri, P. Tomancak, A. Cardona, Fiji: An open-source platform for biological-image analysis. *Nat. Methods.* 9, 676–682 (2012). doi: 10.1038/nmeth.2019
- 31. C. T. Rueden, J. Schindelin, M. C. Hiner, B. E. DeZonia, A. E. Walter, E. T. Arena, K. W. Eliceiri, ImageJ2: ImageJ for the next generation of scientific image data. *BMC Bioinformatics*. **18**, 529 (2017). doi: 10.1186/s12859-017-1934-z

- 32. P. Thévenaz, U. E. Ruttimann, M. Unser, A pyramid approach to subpixel registration based on intensity. *IEEE Trans. Image Process.* **7**, 27–41 (1998). doi: 10.1109/83.650848
- 33. R. E. García, J. Blendell, Equilibrium wulff shape generator (2014), doi:10.21981/D3C53F234.
- 34. A. R. Roosen, R. P. McCormack, W. C. Carter, Wulffman: A tool for the calculation and display of crystal shapes. *Comput. Mater. Sci.* 11, 16–26 (1998). doi: 10.1016/S0927-0256(97)00167-5
- 35. R. Sharma, An environmental transmission electron microscope for in situ synthesis and characterization of nanomaterials. *J. Mater. Res.* **20,** 1695–1707 (2005). doi: 10.1557/JMR.2005.0241
- 36. P. A. Crozier, T. W. Hansen, In situ and operando transmission electron microscopy of catalytic materials. *MRS Bull.* **40**, 38–45 (2015). doi: 10.1557/mrs.2014.304
- 37. D. Zhang, C. Jin, H. Tian, Y. Xiong, H. Zhang, P. Qiao, J. Fan, Z. Zhang, Z. Y. Li, J. Li, An: In situ TEM study of the surface oxidation of palladium nanocrystals assisted by electron irradiation. *Nanoscale*. **9**, 6327–6333 (2017). doi: 10.1039/c6nr08763a
- 38. L. D. Marks, Wiener-filter enhancement of noisy HREM images. *Ultramicroscopy*. **62**, 43–52 (1996). doi: 10.1016/0304-3991(95)00085-2
- 39. R. Kilaas, Optimal and near-optimal filters in high-resolution electron microscopy. *J. Microsc.* **190** (1998), pp. 45–51.
- 40. G. Kresse, J. Furthmüller, Efficiency of ab-initio total energy calculations for metals and

- semiconductors using a plane-wave basis set. *Comput. Mater. Sci.* **6**, 15–50 (1996). doi: 10.1016/0927-0256(96)00008-0
- 41. G. Kresse, J. Furthmüller, Efficient iterative schemes for ab initio total-energy calculations using a plane-wave basis set. *Phys. Rev. B Condens. Matter Mater. Phys.* **54**, 11169–11186 (1996). doi: 10.1103/PhysRevB.54.11169
- 42. J. P. Perdew, K. Burke, M. Ernzerhof, Generalized gradient approximation made simple.

 Phys. Rev. Lett. 77, 3865–3868 (1996). doi: 10.1103/PhysRevLett.77.3865
- 43. S. Grimme, J. Antony, S. Ehrlich, H. Krieg, A consistent and accurate ab initio parametrization of density functional dispersion correction (DFT-D) for the 94 elements H-Pu. *J. Chem. Phys.* **132**, 154104 (2010). doi: 10.1063/1.3382344
- 44. J. Neugebauer, M. Scheffler, Adsorbate-substrate and adsorbate-adsorbate interactions of Na and K adlayers on Al(111). *Phys. Rev. B.* **46**, 16067–16080 (1992). doi: 10.1103/PhysRevB.46.16067
- 45. L. Bengtsson, Dipole correction for surface supercell calculations. *Phys. Rev. B Condens. Matter Mater. Phys.* **59**, 12301–12304 (1999). doi: 10.1103/PhysRevB.59.12301
- 46. H. J. Monkhorst, J. D. Pack, Special points for Brillonin-zone integrations. *Phys. Rev. B*.
 13, 5188–5192 (1976). doi: https://doi.org/10.1103/PhysRevB.13.5188
- 47. K. D. Gilroy, A. O. Elnabawy, T.-H. Yang, L. T. Roling, J. Howe, M. Mavrikakis, Y. Xia, Thermal Stability of Metal Nanocrystals: An Investigation of the Surface and Bulk Reconstructions of Pd Concave Icosahedra. *Nano Lett.* 17, 3655–3661 (2017). doi:

- https://doi.org/10.1021/acs.nanolett.7b00844
- A. L. Mackay, A dense non-crystallographic packing of equal spheres. *Acta Crystallogr*.
 15, 916–918 (1962). doi: https://doi.org/10.1107/S0365110X6200239X
- G. Henkelman, B. P. Uberuaga, H. Jónsson, A climbing image nudged elastic band method for finding saddle points and minimum energy paths. *J. Chem. Phys.* 113, 9901–9904 (2000). doi: 10.1063/1.1329672
- 50. G. Henkelman, H. Jónsson, Improved tangent estimate in the nudged elastic band method for finding minimum energy paths and saddle points. *J. Chem. Phys.* **113**, 9978–9985 (2000). doi: 10.1063/1.1323224
- D. M. Wood, A. Zunger, A new method for diagonalising large matrices. *J. Phys. A. Math. Gen.* 18, 1343–1359 (1985). doi: 10.1088/0305-4470/18/9/018
- 52. C.-M. Niu, P. H. Rieger, K. Dwight, A. Wold, preparation and properties of the system $Cu_xPd_{1-x}O$ (0 <= x <= 0.175). *J. Solid State Chem.* **86**, 175–179 (1990). doi: 10.1016/0022-4596(90)90132-H
- 53. W. M. Haynes, *CRC Handbook of Chemistry and Physics* (CRC Press, New York, ed. 95, 2014).
- 54. M. López Granados, F. C. Galisteo, P. S. Lambrou, R. Mariscal, J. Sanz, I. Sobrados, J. L. G. Fierro, A. M. Efstathiou, Role of P-containing species in phosphated CeO₂ in the deterioration of its oxygen storage and release properties. *J. Catal.* 239, 410–421 (2006). doi: 10.1016/j.jcat.2006.02.007

- 55. T. Montini, M. Melchionna, M. Monai, P. Fornasiero, Fundamentals and catalytic applications of CeO₂-based materials. *Chem. Rev.* **116**, 5987–6041 (2016). doi: 10.1021/acs.chemrev.5b00603
- 56. F. de la Peña, E. Prestat, V. Tonaas Fauske, P. Burdet, P. Jokubauskas, M. Nord, T. Ostasevicius, K. E. MacArthur, M. Sarahan, D. N. Johnstone, J. Taillon, J. Lähnemann, V. Migunov, A. Eljarrat, J. Caron, T. Aarholt, S. Mazzucco, M. Walls, T. Slater, F. Winkler, pquinn-dls, B. Martineau, G. Donval, R. McLeod, E. R. Hoglund, I. Alxneit, D. Lundeby, T. Henninen, L. F. Zagonel, A. Garmannslund, F. de la Peña, E. Prestat, V. Tonaas Fauske, P. Burdet, P. Jokubauskas, M. Nord, T. Ostasevicius, K. E. MacArthur, M. Sarahan, D. N. Johnstone, J. Taillon, J. Lähnemann, V. Migunov, A. Eljarrat, J. Caron, T. Aarholt, S. Mazzucco, M. Walls, T. Slater, F. Winkler, pquinn-dls, B. Martineau, G. Donval, R. McLeod, E. R. Hoglund, I. Alxneit, D. Lundeby, T. Henninen, L. F. Zagonel, A. Garmannslund, hyperspy/hyperspy: HyperSpy v1.5.2. zndo (2019),doi:10.5281/ZENODO.592838.
- 57. J. Han, D. Y. Zemlyanov, F. H. Ribeiro, Interaction of O₂ with Pd single crystals in the range 1-150 Torr: Oxygen dissolution and reaction. *Surf. Sci.* **600**, 2752–2761 (2006). doi: 10.1016/j.susc.2006.04.042

ACKNOWLEDGEMENTS

Funding: This work was mostly supported by NYSEARCH. Additional funding was provided by the Stanford Natural Gas Initiative. T.W., L.X., and M.M. acknowledge support for the computational modeling work by the U.S. Department of Energy, Office of Science, Office of Basic Energy Sciences, Division of Chemical Sciences, Geosciences, and Biosciences (Grant DE-FG02-05ER15731). B.A.R. was supported by the HydroGEN Advanced Water Splitting Consortium, established as part of the Energy Materials Network under the U.S. Department of Energy, Office of Energy Efficiency and Renewable Energy, Hydrogen and Fuel Cell Technologies Office, under Award Number DE-EE-0008084. Part of the experimental work was performed at the Stanford Nano Shared Facilities (SNSF), supported by the National Science Foundation under award no. ECCS-1542152. The computational work was performed in part by using supercomputing resources from the National Energy Research Scientific Computing Center (NERSC), a DOE Office of Science User Facility located at Lawrence Berkeley National Laboratory and operated under contract DE-AC02-05CH11231, and from the Center for Nanoscale Materials, a DOE Office of Science User Facility located at Argonne National Laboratory, supported by DOE contract DE-AC02-06CH11357. A.M.L. acknowledges support from the Department of Energy, Office of Science, Basic Energy Sciences, Materials Sciences and Engineering Division, under Contract DE-AC02-76SF00515. Author contributions: W.H. and M.C. designed the project. W.H. performed catalyst synthesis, characterization, catalytic tests, and data analysis. A.C.J.-P. performed all HR-STEM measurements and the related data analysis. T.W. and L.X. performed theoretical calculations supervised by M.M. W.D.Y. conducted ETEM experiments and data analysis. J.O., B.A.R. and C.Z. conducted catalyst synthesis for laser ablation and the related catalytic tests supervised by A.M.L. M.E.H. and A.A.H. performed the surface strain data analysis. M.C. supervised the project. W.H. prepared a manuscript draft and all authors

contributed to the final manuscript. Competing interests: Stanford University has submitted a

provisional patent application entitled "Promoting catalytic activity through steam treatment-

induced nanoparticles restructuring" on which W.H. and M.C. are listed as inventors (US

provisional patent number 63/084,847). The authors declare no competing financial interests. **Data**

and materials availability: All data needed to evaluate the conclusions in the paper are present

in the paper or the Supplementary Materials.

SUPPLEMENTARY MATERIALS

Materials and Methods

Supplemental Text

Figs. S1 to S38

Tables S1 to S7

References (28-57)

29